

Temporal Goos-Hänchen Shift in Synthetic Discrete-Time Heterolattices


Chengzhi Qin,¹ Shulin Wang,¹ Bing Wang^{1,*}, Xinyuan Hu,¹ Chenyu Liu,¹ Yinglan Li,¹
Lange Zhao,¹ Han Ye,¹ Stefano Longhi^{2,3,†} and Peixiang Lu^{1,4,‡}

¹Wuhan National Laboratory for Optoelectronics and School of Physics,
Huazhong University of Science and Technology, Wuhan 430074, China

²Dipartimento di Fisica, Politecnico di Milano, Piazza Leonardo da Vinci 32, I-20133 Milano, Italy

³IFISC (UIB-CSIC), Instituto de Física Interdisciplinar y Sistemas Complejos, E-07122 Palma de Mallorca, Spain

⁴Hubei Key Laboratory of Optical Information and Pattern Recognition, Wuhan Institute of Technology, Wuhan 430205, China

 (Received 1 April 2024; revised 5 June 2024; accepted 10 July 2024; published 20 August 2024)

Experimental demonstration of tunable temporal Goos-Hänchen shift (GHS) in synthetic discrete-time heterolattices with scalar and vector gauge potentials is reported. By using Heaviside-function modulation in two fiber loops, we create a sharp gauge-potential interface and observe temporal GHS for total internal reflection (TIR), which manifests as a time delay rather than a spatial shift. The TIR occurs as the incident mode falls into the band gap of transmitted region with band shifting by scalar and vector potential. We find that both scalar and vector potential codetermine GHS by controlling the decay (imaginary part) and oscillation (real part) of a penetrated evanescent wave, in stark contrast to traditional spatial GHS only determined by the decay factor. We also observe diverging characteristics of GHS at band-gap edges where evanescent-to-propagating wave transition occurs. GHS for frustrated total internal reflection (FTIR) by a finite-width evanescent barrier is also demonstrated, which shows saturation properties to the single-interface TIR case under infinite-width limit. Finally, we develop an accumulation measurement method using multiple TIRs to improve the precision for measuring even tinier GHS. The study initiates precise measurement of temporal GHS for discrete-time reflections, which may feature potential applications in precise time-delay control and measurement.

DOI: [10.1103/PhysRevLett.133.083802](https://doi.org/10.1103/PhysRevLett.133.083802)

Introduction—Goos-Hänchen shift (GHS) [1] refers to a spatial beam displacement relative to its geometric center upon total internal reflection (TIR) at two media's interface. The existence of GHS indicates more precision of wave optics over ray optics in describing light propagation in dielectric media [2–4], with some key applications in optical sensing and interferometry [5–7]. Since GHS is essentially an interference effect, it arises in many other wave systems beyond optics, including electron waves [8,9], neutrons [10], spin waves [11], matter waves [12,13], and Weyl media [14–16]. Besides in continuous media, GHS has been also extended to structured media like photonic crystals [7,17–21], waveguide arrays [22,23], subwavelength gratings [24,25], and metamaterials [26]. However, all these studies have been limited to spatial interfaces, where GHS manifests as a purely spatial displacement that usually cannot be tuned or reconfigured once the media or structures have been fabricated. Inspired by recent interest in studying temporal boundary effects, including time reflection and refraction [27–30], temporal

light guiding [31,32] and time crystals [33–35], there also emerges a theoretical proposal on realizing temporal GHS at continuous time boundary created via an abrupt change of the medium's refractive index [36]. However, continuous temporal boundaries usually require very fast and large index modulations, which are challenging to realize in experiment. Alternatively, discrete temporal boundaries can also be created in synthetic temporal lattices using fiber-loop circuits [37–42]. Without relying on real material's index change, discrete time boundaries are created by introducing scalar and/or vector potential steps, which can be readily synthesized and reconfigured through external modulations. Since the real timescales of synthetic lattices are defined by fiber-loop lengths, they can also be flexibly scaled up or down to fit high-speed modulation demands.

In this Letter, we theoretically propose and experimentally demonstrate tunable temporal GHS at gauge-potential interfaces created in discrete temporal lattices. We show that scalar and vector potentials can induce a vertical and horizontal band shift, enabling the creation of a potential step via Heaviside-function modulation. As the incident mode falls into the band gap of the transmitted region, temporal TIR occurs and GHS is generated. We find both scalar and vector potential codetermine GHS by controlling

*Contact author: wangbing@hust.edu.cn

†Contact author: stefano.longhi@polimi.it

‡Contact author: lupeixiang@hust.edu.cn

evanescent-wave decay and oscillation tails, with a giant GHS reached at band-gap edges. We also measure GHS by frustrated total internal reflection (FTIR) by a finite-width evanescent barrier, which increases with barrier width and saturates at infinite-width limit of single-interface case. Finally, an accumulation measurement technique using multiple TIRs is proposed and demonstrated, which can provide accurate measurements of very tiny GHS.

GHS for temporal TIR—To observe temporal GHS, we synthesize a discrete-time heterolattice using pulse evolutions in two coupled fiber loops [Fig. 1(a)], where light dynamics is described by the discretized iteration equations [37–42]

$$\begin{aligned} u_n^m &= [\cos(\beta)u_{n+1}^{m-1} + i \sin(\beta)v_{n+1}^{m-1}]e^{i\phi_u} \\ v_n^m &= [i \sin(\beta)u_{n-1}^{m-1} + \cos(\beta)v_{n-1}^{m-1}]e^{i\phi_v}, \end{aligned} \quad (1)$$

where u_n^m , v_n^m are pulse amplitudes in leftward or rightward path towards the node at site n and step m , β ($0 < \beta < \pi/2$) is the coupling angle of central coupler, corresponding to a splitting ratio of $\cos^2(\beta)/\sin^2(\beta)$. The additional phase shifts ϕ_u , ϕ_v in short or long loops are associated to a scalar φ and vector potential A through Peierls' substitution [43–46]: $\phi_u = \int_{m-1}^m \varphi dm + \int_{n+1}^n A dn = \varphi - A$,

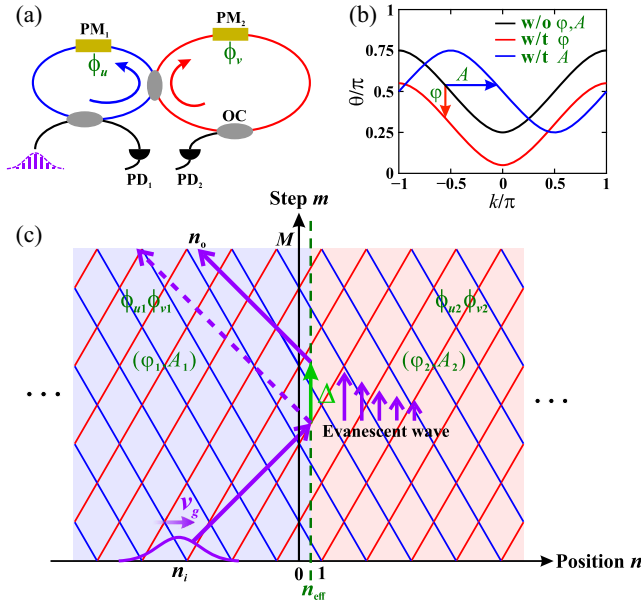


FIG. 1. (a) Sketch of two coupled fiber loops to realize synthetic temporal lattice. PM: phase modulator; PD: photon detector; OC: optical coupler. (b) Schematic band shift by scalar potential $\varphi = \pi/5$ or vector potential $A = \pi/2$ under $\beta = \pi/4$. (c) Discrete-time heterolattice with gauge-potential distribution (φ_1, A_1) , (φ_2, A_2) using nonuniform phase modulations (ϕ_{u1}, ϕ_{v1}) , (ϕ_{u2}, ϕ_{v2}) , with interface locating at $n_{\text{eff}} = 0.5$. The input, output packets' positions are n_i , n_o and total evolution step is $m = M$. The dashed arrow denotes geometric-optics-predicted beam center. $v_g(k_i)$ denotes group velocity of the incident packet. GHS is denoted by Δ .

$\phi_v = \int_{m-1}^m \varphi dm + \int_{n-1}^n A dn = \varphi + A$, which yields $\varphi = (\phi_v + \phi_u)/2$, $A = (\phi_v - \phi_u)/2$. For a homogeneous lattice with uniform ϕ_u , ϕ_v , the Bloch eigenstate is $(u_n^m, v_n^m)^T = \psi e^{ikn} e^{-i\theta m}$, where $\psi = (U, V)^T$ is eigenvector, k is the transverse Bloch momentum, and θ is the longitudinal propagation constant (quasienergy) defined by Floquet band structure $\theta_{\pm}(k) = \pm \cos^{-1}[\cos(\beta) \cos(k - A)] - \varphi$, “ \pm ” denote upper and lower band branches. The vector and scalar potentials can thus induce horizontal and vertical band shifts, respectively [Fig. 1(b)]. Note that the Floquet band has two band gaps: a “0-gap” between $-\beta < \theta < \beta$ centered at $\theta = 0$ and a “ π -gap” between $\pi - \beta < \theta < \pi$ or $-\pi < \theta < -\pi + \beta$ centered at $\theta = \pi$ [Fig. 2(a)], which are responsible for temporal TIR and GHS.

To induce TIR, we create a gauge-potential interface between $n = 0$ and $n = 1$, corresponding to a gauge-potential distribution $(\varphi_1, A_1) = (0, 0)$ for $n \leq 0$ and $(\varphi_2, A_2) = (\Delta\varphi, \Delta A)$ for $n \geq 1$ [Fig. 1(c)], where $\Delta\varphi$, ΔA are scalar and vector potential steps. Consider a Bloch wave packet at (k_i, θ_i) in “+” band incident from the left side, it will excite reflected and transmitted packets at (k_r, θ_r) and (k_t, θ_t) , which generically read

$$\psi(n, m) = \begin{cases} (\psi_i e^{ik_i n} + r \psi_r e^{ik_r n}) e^{-i\theta_i m} & (n \leq 0) \\ t \psi_t e^{ik_t n} e^{-i\theta_t m} & (n \geq 1) \end{cases}, \quad (2)$$

where r , t are reflected and transmitted coefficients, ψ_i , ψ_r , and ψ_t are eigenvectors of incident, reflected, and transmitted packets: $\psi_i = \psi(k_i)_+ = [1, -e^{\lambda_i} e^{-ik_i}]^T / \sqrt{1 + e^{2\lambda_i}}$, $\psi_r = \psi(k_r)_+ = [1, -e^{\lambda_r} e^{-ik_r}]^T / \sqrt{1 + e^{2\lambda_r}}$, $\psi_t = \psi(k_t)_{\pm} = [1, \mp e^{\pm \lambda_t} e^{-i(k_t - \Delta A)}]^T / \sqrt{1 + e^{\pm 2\lambda_t}}$, $\lambda_{i,r} = \sinh^{-1}[\cot(\beta) \times \sin(k_{i,r})]$, $\lambda_t = \sinh^{-1}[\cot(\beta) \sin(k_t - \Delta A)]$, and $\theta_{i,r} = \cos^{-1}[\cos(\beta) \cos(k_{i,r})]$, $\theta_t = \cos^{-1}[\cos(\beta) \cos(k_t - \Delta A)] - \Delta\varphi$.

To determine k_t , according to Snell's law, i.e., conservation of tangential momentum (propagation constant) parallel to the m axis, $\theta_i = \theta_r = \theta_t$, one obtains

$$\cos(\beta) \cos(k_t - \Delta A) = \cos(\theta_i + \Delta\varphi). \quad (3)$$

Throughout the Letter we choose $\Delta\varphi < 0$, so that the right-side band is shifted upward with respect to left one. This analysis is also applicable to $\Delta\varphi > 0$. As we continuously increase $-\Delta\varphi$ from 0 to 2π [Fig. 2(a)], θ_i will fall into the 0 gap and π gap when $(\theta_i - \beta) < -\Delta\varphi < (\theta_i + \beta)$ and $(\theta_i - \beta + \pi) < -\Delta\varphi < (\theta_i + \beta + \pi)$. For both cases, TIR occurs and the transmitted packet becomes an evanescent wave, which possesses a complex-valued Bloch momentum

$$k_t = \begin{cases} \Delta A + ik, & (0\text{-gap}) \\ \Delta A + \pi + ik, & (\pi\text{-gap}) \end{cases}, \quad (4)$$

where $\kappa = \cosh^{-1}[\cos(\theta_i + \Delta\varphi)/\cos(\beta)]$ in 0-gap and $\kappa = \cosh^{-1}[-\cos(\theta_i + \Delta\varphi)/\cos(\beta)]$ in the π gap. In

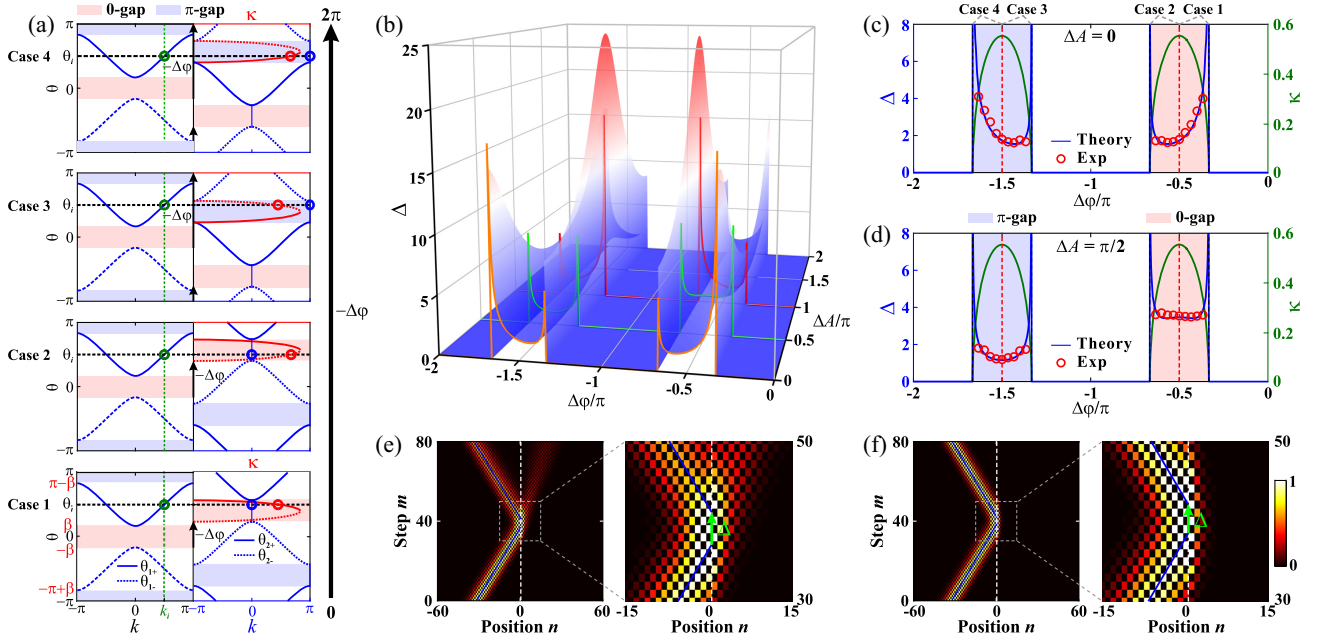


FIG. 2. (a) Band matching for left- and right-side regions as $-\Delta\varphi$ increase continuously from 0 to 2π under $\Delta A = 0$. (b) Theoretical GHS versus $\Delta\varphi$ and ΔA , where orange, green, and red curves denote $\Delta A = 0, \pi/2$, and π . (c),(d) Theoretical and measured GHS for $\Delta A = 0, \pi/2$. (e),(f) Measured packet's evolutions for $\Delta A = 0, \Delta\varphi = -0.366\pi$, and $\Delta A = \pi/2, \Delta\varphi = -0.5\pi$ under $\beta = \pi/6$.

contrast to the traditional spatial evanescent wave taking a purely decay shape $\sim e^{-kn}$ [1–26], the temporal evanescent wave manifests a simultaneously oscillatory decay shape $\sim e^{i\Delta A n} e^{-kn}$, where the oscillation and decay constants are determined by vector and scalar potential differences, respectively. More explicitly, there totally exist 4 cases where ψ_t belongs to, case 1: “+” band in 0 gap; case 2: “-” band in 0 gap; case 3: “-” band in π gap; and case 4: “+” band in π gap, as shown from bottom to top panels in Fig. 2(a), where “+/-” is chosen for cases 1, 4 and 2, 3.

The reflection coefficient r can be obtained by imposing wave function continuity of U at $n = 0$ and V at $n = 1$ [41],

$\psi_i + r\psi_r = t\psi_t$, $\psi_i e^{ik_i} + r\psi_r e^{ik_r} = t\psi_t e^{ik_t}$, yielding

$$r_{\pm} = \frac{\pm 1 - e^{\pm\lambda_t - \lambda_i + i\Delta A}}{e^{\pm\lambda_t + i\Delta A} \mp e^{-\lambda_i}}, \quad (5)$$

where “+/-” is chosen for cases 1, 4 and 2, 3 with “-/+” chosen in “ \mp ” (same below). Since TIR occurs, r_{\pm} must be unimodular and can be rewritten as $r_{\pm} = e^{i\phi_{\pm}}$, where $\phi_{\pm} = -i \ln(r_{\pm})$ is the reflection phase. GHS is calculated using Artman's stationary-phase method: $\Delta_{\pm} \equiv \partial\phi_{\pm}/\partial\theta|_{\theta=\theta_i} = -i(\partial r_{\pm}/\partial\theta)/r_{\pm}|_{\theta=\theta_i}$, [8,20–23], which reads (see Supplemental Material, Sec. II for derivation [47])

$$\Delta_{\pm} = -i \frac{(e^{\pm 2\lambda_t - \lambda_i + i2\Delta A} - e^{-\lambda_i})\partial\lambda_i/\partial\theta + (e^{\pm\lambda_t - 2\lambda_i + i\Delta A} - e^{\pm\lambda_t + i\Delta A})\partial\lambda_t/\partial\theta}{(\pm 1 - e^{\pm\lambda_t - \lambda_i + i\Delta A})(e^{\pm\lambda_t + i\Delta A} \mp e^{-\lambda_i})} \Big|_{\theta=\theta_i}. \quad (6)$$

Here $\partial\lambda_i/\partial\theta = \cos(\theta)/\sqrt{\cos^2(\beta) - \cos^2(\theta)}$, $\partial\lambda_t/\partial\theta = \pm \cos(\theta + \Delta\varphi)/\sqrt{\cos^2(\beta) - \cos^2(\theta + \Delta\varphi)}$, in $\partial\lambda_i/\partial\theta$, “+/-” is chosen for cases 1, 3 and 2, 4. The behavior of GHS versus $\Delta\varphi$ and ΔA is shown in Fig. 2(b). As expected, GHS is nonvanishing only within the band gaps, which is larger near band-gap edges than band-gap centers. Specifically, as $\theta_i + \Delta\varphi = \pm\beta$ (or $\pi \pm \beta$) at 0-gap or π -gap edges, the term $\partial\lambda_t/\partial\theta$ and hence GHS diverges at the critical points where evanescent-to-propagative wave transition occurs. However, such a diverging behavior is unphysical and disappears when we consider the full scattering problem of a finite-width packet obtained from

superposition (integral) of wave numbers near a carrier k . Since near the critical point the phase ϕ changes rapidly as θ is varied, strong wave packet distortion occurs and stationary-phase analysis breaks down, making the GHS expression $\Delta \equiv \partial\phi/\partial\theta$ invalid [36] (more details are given in Supplemental Material [47], Sec. II).

The theoretical analysis has been verified by our reflection experiments based on two fiber loops. The gauge-potential interface is created by applying a Heaviside modulation from $(\phi_{u1}, \phi_{v1}) = (0, 0)$ to $(\phi_{u2}, \phi_{v2}) = (\Delta\varphi - \Delta A, \Delta\varphi + \Delta A)$ between $n = 0$ and $n = 1$. The real time intervals of m and n axes are $T_m \sim 25 \mu\text{s}$, $\Delta t \sim 75 \text{ ns}$

by choosing two-loop lengths $L \sim 5 \text{ km} \pm 15 \text{ m}$, which allow abrupt jump of the electro-optical modulation signal at $\sim \text{ns}$ speed. Details of the experimental setup and key techniques are discussed in Supplemental Material [47], Sec. I. We record the packet's input and output positions n_i , n_o and total evolution step M . According to $(n_{\text{eff}} - n_i)/|v_g(k_i)| + (n_{\text{eff}} - n_o)/|v_g(k_r)| + \Delta_{\text{exp}} = M$ and equal packet's group velocities $|v_g(k_i)| = |v_g(k_r)|$ for $k_r = -k_i$, we can retrieve the experimentally measured GHS

$$\Delta_{\text{exp}} = M - \frac{2n_{\text{eff}} - n_i - n_o}{|v_g(k_i)|}, \quad (7)$$

where $n_{\text{eff}} = 0.5$ is the effective boundary position between $n = 0$ and $n = 1$.

The measured GHS versus $\Delta\varphi$ for representative $\Delta A = 0$ and $\pi/2$ are denoted by red circles in Figs. 2(c) and 2(d), which agree fairly with theoretical predictions by Eq. (6). Here we choose $\beta = \pi/6$, $\theta_i = \pi/2$ for $k_i = \pi/2$. The two cases have different GHS although they share the same κ (green curves). For $\Delta A = 0$, GHS is symmetric in two

band gaps while asymmetric in each gap, showing diverging (giant) characteristics at band-gap edges. While for $\Delta A = \pi/2$, GHS becomes symmetric in each gap. Figure 2(e) shows field evolution for $\Delta\varphi = -0.366\pi$, $\Delta A = 0$. The experimentally measured GHS is $\Delta_{\text{exp}} \sim 4$, corresponding to a real time delay of $\sim 4T_m = 100 \mu\text{s}$. For $\Delta\varphi = -0.5\pi$, $\Delta A = 0.5\pi$ [Fig. 2(f)], we get $\Delta_{\text{exp}} \sim 3.7$. Theoretical and simulated GHS results for other gauge-potential cases are discussed in Supplemental Material [47], Sec. II.

GHS for temporal FTIR—We argue that GHS can also exist for temporal FTIR by a finite-width gauge-potential barrier. FTIR is an optical analog of quantum tunneling effect through an evanescent barrier sandwiched by two propagative-wave regions, which shows the exponential damping tunneling probability (transmittance) with respect to the barrier's width [48–53] and superluminal tunneling times via the Hartman effect [48,49,54–56]. To inspect how exponential tunneling affects GHS, we consider a potential barrier $\varphi_2 = \Delta\varphi$, $A_2 = 0$ within $1 \leq n \leq W$, and $\varphi_1 = \varphi_3 = 0$, $A_1 = A_3 = 0$ outside, where W is the barrier width. The wave functions in the three regions $s = 1, 2, 3$ are

$$\psi(n, m) = \begin{cases} (\psi_{1i} e^{ik_{1i}n} + r_1 \psi_{1r} e^{ik_{1r}n}) e^{-i\theta_i m}, & (s = 1, n \leq 0) \\ (t_2 \psi_{2t} e^{ik_{2t}n} + r_2 \psi_{2r} e^{ik_{2r}n}) e^{-i\theta_i m}, & (s = 2, 1 \leq n \leq W) \\ t_3 \psi_{3t} e^{ik_{3t}n} e^{-i\theta_i m}, & (s = 3, n \geq W + 1) \end{cases}, \quad (8)$$

where t_s, r_s are amplitudes of forward and backward waves ψ_{st}, ψ_{sr} in region s (see Supplemental Material [47], Sec. III for explicit forms), k_{st}, k_{sr} are Bloch momenta, $-\lambda_{sr} = \lambda_{st} = \sinh^{-1}[\cot(\beta) \sin(k_{st} - A_s)]$. With similar procedures of applying wave function continuities at $n = 0, 1$ and $n = W, W + 1$, we can obtain the reflection and transmission coefficients (see Supplemental Material [47], Sec. III for derivation)

$$r_{1,\pm} = \frac{1 - \rho_{\pm} e^{-\lambda_{1i}}}{\rho_{\pm} - e^{-\lambda_{1i}}}, \quad t_{3,\pm} = \frac{e^{ik_{2t}W}}{e^{ik_{3t}W}} \left[1 + \left(\frac{e^{\pm\lambda_{2r}} \mp e^{\lambda_{1r}}}{e^{\pm\lambda_{2r}} \mp e^{\lambda_{3t}}} \right) e^{\lambda_{1i}} r_{1,\pm} \right], \quad (9)$$

where the barrier-width factor is given by

$$\rho_{\pm} = \frac{(\pm e^{\lambda_{3t}} - e^{\pm\lambda_{2t}}) e^{-2\kappa W} e^{\pm\lambda_{2r}} \mp (e^{\lambda_{3t}} \mp e^{\pm\lambda_{2r}}) e^{\pm\lambda_{2t}}}{(e^{\lambda_{3t}} \mp e^{\pm\lambda_{2t}}) e^{-2\kappa W} - (e^{\lambda_{3t}} \mp e^{\pm\lambda_{2r}})}. \quad (10)$$

GHS is still calculated using stationary-phase analysis: $\Delta_{\pm} = -i(\partial r_{1,\pm}/\partial\theta)/r_{1,\pm}|_{\theta=\theta_i}$. The transmittance is $T = |t_{3,\pm}|^2 \propto e^{-2\kappa W}$, showing characteristic exponential decay with barrier width W . Specifically, in the infinite-width limit $W \rightarrow \infty$, $e^{-2\kappa W} \rightarrow 0$, $\rho_{\pm} = \pm e^{\pm\lambda_{2t}}$, $r_{1,\pm} = (\pm 1 - e^{\pm\lambda_{2t} - \lambda_{1i}})/(e^{\pm\lambda_{2t}} \mp e^{-\lambda_{1i}})$, which reduces to single-interface

case in Eq. (5). Accordingly, $T \rightarrow 0$ and GHS reduces to single-interface case.

The measured T and GHS versus $\Delta\varphi$ for representative $W = 1, 2$, and 5 are shown in Figs. 3(a) and 3(b). T decreases with W while GHS increases with W , both saturating at single-interface limit $W \rightarrow \infty$. These trends can be explained from forward-backward evanescent-wave interference analysis (Supplemental Material [47], Sec. IV): forward-backward waves are out-of-phase with one another, their destructive interference makes GHS smaller than the single-interface case. Since $r_2/t_2 \propto e^{-2\kappa W}$, the weight factor of the backward wave decreases exponentially with W , leading to an increase of GHS with W . When $W \rightarrow \infty$, $r_2 \rightarrow 0$, the backward wave nearly vanishes, making GHS reduce to the single-interface TIR case. Figure 3(c) shows T and GHS for $\Delta\varphi = -0.4\pi$, where T follows the characteristic $\sim e^{-2\kappa W}$ law of the quantum tunneling effect [48–53]. Figures 3(d)–3(f) show the packet's evolutions for $W = 1, 2, 5$, and $\Delta\varphi = -0.4\pi$, where T decreases with W and $\Delta_{\text{exp}} = 1.06, 1.95$, and 3.13 , respectively.

Accumulated measurement of very tiny GHS—For even tinier GHS, its measurement can be easily influenced by parameters measuring precision. To improve the measurement precision, we propose an accumulation measurement method using multiple TIRs to probe averaging rather than one-time GHS. As sketched in Fig. 4(a), we design a

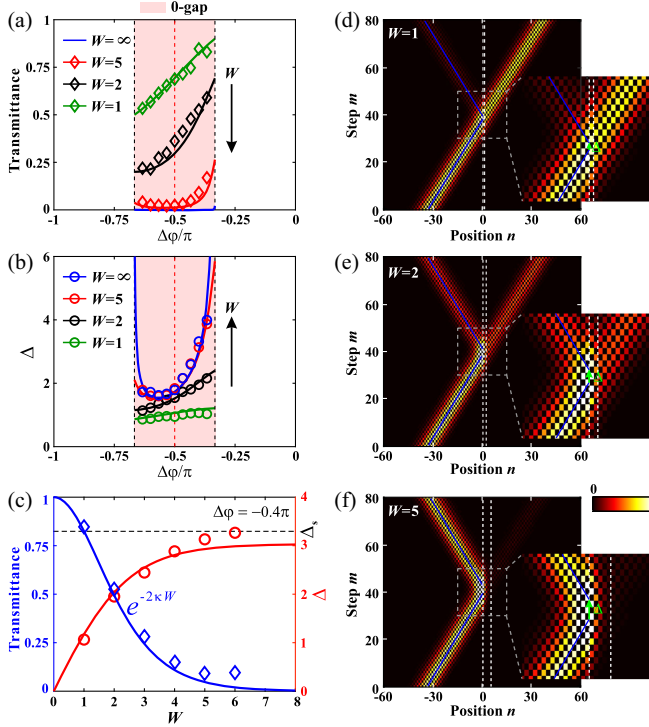


FIG. 3. (a) Theoretical and measured transmittances versus $\Delta\phi$ for a gauge-potential barrier with width $W = 1, 2, 5$ and ∞ (single-interface case). (b) Theoretical and measured GHS versus $\Delta\phi$ for $W = 1, 2, 5$ and ∞ . (c) Transmittance and GHS versus W under $\Delta\phi = -0.4\pi$. (d)–(f) Measured packet's evolutions for $W = 1, 2, 5$ with $\Delta\phi = -0.4\pi$, $\beta = \pi/6$.

temporal waveguide structure composed of a propagative-wave core sandwiched by two evanescent claddings. By denoting n_1, n_2 the left and right boundaries, $W = n_2 - n_1$ the core width and N the total reflection times, we can obtain the averaging GHS

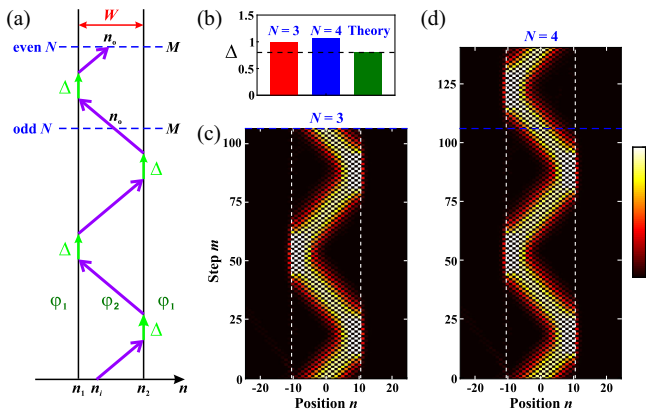


FIG. 4. (a) Schematic temporal waveguide with multiple TIRs for accumulated measurement of GHS. Input, output packets' positions and two boundaries are n_i, n_o and n_1, n_2 , with width $W = n_2 - n_1$. N, M are total reflection times and evolution steps. (b) Measured GHS for $N = 3, 4$ and theoretical GHS. (c), (d) Measured packet's evolutions for $N = 3, 4$ and $\beta = \pi/3.5$.

$$\Delta_{\text{exp}} = \begin{cases} \frac{1}{N} \left[M - \frac{(N-1)W + 2n_2 - n_o - n_i}{|v_g(k_i)|} \right], & (\text{odd } N) \\ \frac{1}{N} \left[M - \frac{NW + n_o - n_i}{|v_g(k_i)|} \right], & (\text{even } N) \end{cases} \quad (11)$$

Note that for $N = 1$, Eq. (11) reduces to one-time reflection case of Eq. (7) with n_2 acting as the single interface. The measured field evolutions after odd $N = 3$ and even $N = 4$ reflections are shown in Figs. 4(c) and 4(d), where $\beta = \pi/3.5$, $\Delta\phi = -0.5\pi$, $\Delta A = 0$. The averaging GHS is $\Delta_{\text{exp}} \sim 1$ for $N = 3, 4$ in Fig. 4(b), which agrees well with theoretical value of $\Delta \sim 0.8$.

Conclusion—In summary, we reported on the first experimental demonstration of tunable temporal GHS at gauge-potential interfaces, which manifests as a temporal beam delay rather than a spatial shift. Unlike ordinary spatial GHS, temporal GHS is affected by both scalar and vector potentials via decay and oscillatory tails of evanescent waves. By measuring GHS for FTIR by a finite-width gauge-potential barrier, we find a wider potential barrier can boost GHS, which saturates at infinite-width limit of single-interface case. Finally, we develop an accumulated measurement technique to precisely probe very tiny GHS. Our experimental work pushes the GHS concept into the temporal domain exploiting tunable scalar and vector gauge fields, which may feature applications in precise time control and measurement for optical communications, signal processing, and optical sensing.

Acknowledgments—The work is supported by the National Natural Science Foundation of China (No. 12204185, No. 12374305, No. 62305122, and No. 12021004), and Natural Science Foundation of Hubei Province (No. 2022CFB036). S. L. acknowledges the Spanish State Research Agency, through the Severo Ochoa and Maria de Maeztu Program for Centers and Units of Excellence (MDM-2017-0711).

C. Q. and S. W. contributed equally to this Letter.

- [1] F. Goos and H. Hänchen, *Ann. Phys. (N.Y.)* **436**, 333 (1947).
- [2] R. H. Renard, *J. Opt. Soc. Am.* **54**, 1190 (1964).
- [3] K Y Bliokh and A Aiello, *J. Opt.* **15**, 014001 (2013).
- [4] H. Schomerus and M. Hentschel, *Phys. Rev. Lett.* **96**, 243903 (2006).
- [5] F. de Fornel, *Evanescent Waves: From Newtonian Optics to Atomic Optics* (Springer, Berlin, 2001).
- [6] X. Yin and L. Hesselink, *Appl. Phys. Lett.* **89**, 261108 (2006).
- [7] I. V. Soboleva, V. V. Moskalenko, and A. A. Fedyanin, *Phys. Rev. Lett.* **108**, 123901 (2012).
- [8] C. W. J. Beenakker, R. A. Sepkhanov, A. R. Akhmerov, and J. Tworzydło, *Phys. Rev. Lett.* **102**, 146804 (2009).

- [9] Z. Wu, F. Zhai, F. M. Peeters, H. Q. Xu, and K. Chang, *Phys. Rev. Lett.* **106**, 176802 (2011).
- [10] Victor-O. de Haan, T. M. Rekveldt, W. H. Kraan, A. A. van Well, R. M. Dalgliesh, and S. Langridge, *Phys. Rev. Lett.* **104**, 010401 (2010).
- [11] Y. S. Dadoenkova, N. N. Dadoenkova, I. L. Lyubchanskii, M. L. Sokolovskyy, J. W. Klos, J. Romero-Vivas, and M. Krawczyk, *Appl. Phys. Lett.* **101**, 042404 (2012).
- [12] J. Huang, Z. Duan, H. Y. Ling, and W. Zhang, *Phys. Rev. A* **77**, 063608 (2008).
- [13] S.-Y. Lee, J. L. Deunff, M. Choi, and R. Ketzmerick, *Phys. Rev. A* **89**, 022120 (2014).
- [14] Q. D. Jiang, H. Jiang, H. Liu, Q. F. Sun, and X. C. Xie, *Phys. Rev. Lett.* **115**, 156602 (2015).
- [15] U. Chattopadhyay, L. K. Shi, B. Zhang, J. C. W. Song, and Y. D. Chong, *Phys. Rev. Lett.* **122**, 066602 (2019).
- [16] Y. Liu, Z. M. Yu, C. Xiao, and S. A. Yang, *Phys. Rev. Lett.* **125**, 076801 (2020).
- [17] D. Felbacq, A. Moreau, and R. Smaali, *Opt. Lett.* **28**, 1633 (2003).
- [18] D. Felbacq and R. Smaali, *Phys. Rev. Lett.* **92**, 193902 (2004).
- [19] J. He, J. Yi, and S. He, *Opt. Express* **14**, 3024 (2006).
- [20] M. Miri, A. Naqavi, A. Khavasi, K. Mehrany, S. Khorasani, and B. Rashidian, *Opt. Lett.* **33**, 2940 (2008).
- [21] S. Longhi, G. Della Valle, and K. Staliunas, *Phys. Rev. A* **84**, 042119 (2011).
- [22] M. C. Rechtsman, Y. V. Kartashov, F. Setzpfandt, H. Trompeter, L. Torner, T. Pertsch, U. Peschel, and A. Szameit, *Opt. Lett.* **36**, 4446 (2011).
- [23] S. Grosche, A. Szameit, and M. Ornigotti, *Phys. Rev. A* **94**, 063831 (2016).
- [24] F. Wu, J. Wu, Z. Guo, H. Jiang, Y. Sun, Y. Li, J. Ren, and H. Chen, *Phys. Rev. Appl.* **12**, 014028 (2019).
- [25] N. I. Petrov, V. A. Danilov, V. V. Popov, and B. A. Usievich, *Opt. Express* **28**, 7552 (2020).
- [26] P. R. Berman, *Phys. Rev. E* **66**, 067603 (2002).
- [27] B. W. Plansinis, W. R. Donaldson, and G. P. Agrawal, *Phys. Rev. Lett.* **115**, 183901 (2015).
- [28] H. Moussa, Y. Ra'di, G. Xu, S. Yin, and A. Alù, *Nat. Phys.* **19**, 863 (2023).
- [29] E. Galiffi, G. Xu, S. Yin, H. Moussa, Y. Ra'di, and A. Alù, *Nat. Phys.* **19**, 1703 (2023).
- [30] Z. Dong, H. Li, T. Wan, Q. Liang, Z. Yang, and B. Yan, *Nat. Photonics* **18**, 68 (2023).
- [31] B. W. Plansinis, W. R. Donaldson, and G. P. Agrawal, *J. Opt. Soc. Am. B* **33**, 1112 (2016).
- [32] J. Zhou, G. Zheng, and J. Wu, *Phys. Rev. A* **93**, 063847 (2016).
- [33] E. Lustig, Y. Sharabi, and M. Segev, *Optica* **5**, 1390 (2018).
- [34] Y. Sharabi, E. Lustig, and M. Segev, *Phys. Rev. Lett.* **126**, 163902 (2021).
- [35] M. Lyubarov, Y. Lumer, A. Dikopoltsev, E. Lustig, Y. Sharabi, and M. Segev, *Science* **377**, 425 (2022).
- [36] S. A. Ponomarenko, J. Zhang, and G. P. Agrawal, *Phys. Rev. A* **106**, L061501 (2022).
- [37] S. Weidemann, M. Kremer, T. Helbig, T. Hofmann, A. Stegmaier, M. Greiter, R. Thomale, and A. Szameit, *Science* **368**, 311 (2020).
- [38] S. Weidemann, M. Kremer, S. Longhi, and A. Szameit, *Nature (London)* **601**, 354 (2022).
- [39] A. L. M. Muniz, F. O. Wu, P. S. Jung, M. Khajavikhan, D. N. Christodoulides, and U. Peschel, *Science* **379**, 1019 (2023).
- [40] S. Wang *et al.*, *Nat. Commun.* **13**, 7653 (2022).
- [41] H. Ye, C. Qin, S. Wang, L. Zhao, W. Liu, B. Wang, S. Longhi, and P. Lu, *Proc. Natl. Acad. Sci. U.S.A.* **120**, e2300860120 (2023).
- [42] S. Wang, C. Qin, L. Zhao, H. Ye, S. Longhi, P. Lu, and B. Wang, *Sci. Adv.* **9**, eadh0415 (2023).
- [43] Y. Aharonov and D. Bohm, *Phys. Rev.* **115**, 485 (1959).
- [44] K. Fang, Z. Yu, and S. Fan, *Phys. Rev. Lett.* **108**, 153901 (2012).
- [45] K. Fang, Z. Yu, and S. Fan, *Nat. Photonics* **6**, 782 (2012).
- [46] C. Qin, F. Zhou, Y. Peng, D. Sounas, X. Zhu, B. Wang, J. Dong, X. Zhang, A. Alù, and P. Lu, *Phys. Rev. Lett.* **120**, 133901 (2018).
- [47] See Supplemental Material at <http://link.aps.org/supplemental/10.1103/PhysRevLett.133.083802> for details on experimental setup and key measurement techniques, derivation of GHS for TIR at a single gauge-potential interface, derivation of GHS, and transmittance for FTIR by a gauge-potential barrier and evanescent-wave interference analysis for FTIR.
- [48] H. G. Winful, *Phys. Rev. Lett.* **91**, 260401 (2003).
- [49] H. G. Winful and C. Zhang, *Phys. Rev. A* **79**, 023826 (2009).
- [50] X. Chen, X.-J. Lu, P.-L. Zhao, and Q.-B. Zhu, *Opt. Lett.* **37**, 1526 (2012).
- [51] G. M. Gehring, A. C. Liapis, and R. W. Boyd, *Phys. Rev. A* **85**, 032122 (2012).
- [52] G. M. Gehring, A. C. Liapis, S. G. Lukishova, and R. W. Boyd, *Phys. Rev. Lett.* **111**, 030404 (2013).
- [53] M. L. N. Chen, Y. Bi, H.-C. Chan, Z. Lin, S. Ma, and S. Zhang, *Phys. Rev. Lett.* **129**, 123901 (2022).
- [54] V. S. Olkhovskiy and E. Recami, *Phys. Rep.* **214**, 339 (1992).
- [55] H. G. Winful, *Phys. Rep.* **436**, 1 (2006).
- [56] S. Longhi, P. Laporta, M. Belmonte, and E. Recami, *Phys. Rev. E* **65**, 046610 (2002).